Mapping degenerate vortex states in a kagomé lattice of elongated antidots via scanning Hall probe microscopy

Cun Xue,[1,2] Jun-Yi Ge,[2] An He,[3] Vyacheslav S. Zharinov,[2] V. V. Moshchalkov,[2] Y. H. Zhou,[4,5] A. V. Silhanek,[6] and J. Van de Vondel[2]

[1]*School of Mechanics, Civil Engineering and Architecture, Northwestern Polytechnical University, Xi'an 710072, China*
[2]*INPAC–Institute for Nanoscale Physics and Chemistry, KU Leuven, Celestijnenlaan 200D, B–3001 Leuven, Belgium*
[3]*College of science, Chang'an University, Xi'an 710064, China*
[4]*School of Aeronautics, Northwestern Polytechnical University, Xi'an 710072, P. R. China*
[5]*Key Laboratory of Mechanics on Disaster and Environment in Western China attached to the Ministry of Education of China, and Department of Mechanics and Engineering Sciences, Lanzhou University, Lanzhou 730000, China*
[6]*Experimental Physics of Nanostructured Materials, Q-MAT, CESAM, Université de Liège, B-4000 Sart Tilman, Belgium.*

(Dated: April 20, 2017)

We investigate the degeneracy of the superconducting vortex matter ground state by directly visualizing the vortex configurations in a kagomé lattice of elongated antidots via scanning Hall probe microscopy (SHPM). The observed vortex patterns, at specific applied magnetic fields, are in good agreement with the configurations obtained using time-dependent Ginzburg-Landau (TDGL) simulation. Both results indicate that the long range interaction in this nano-structured superconductor is unable to lift degeneracy between different vortex states and the pattern formation is mainly ruled by the nearest neighbour interaction. This simplification allows the identification of a set of simple rules characterizing the vortex configurations. We demonstrated that these rules can explain both the observed vortex distributions and the magnetic field dependent degree of degeneracy.

I. INTRODUCTION

The physics of quantized units of flux in a superconductor interacting with a pinning landscape continues to attract considerable academic interest due to the implications largely transcending the domain of superconductivity such as Bose-condensates [1, 2], colloids [3, 4], semiconductors [5, 6], Mott insulator transition [7], vortex ice and charge ice [10–12], skyrmions [13, 14], cold-atoms trapping [15], etc. The appeal and advantage of superconducting systems is that the size and number of the particles can be tuned by respectively changing the temperature and the strength of the magnetic field. In addition, the enormous flexibility in the design and fabrication of artificial vortex traps in superconducting films has fueled during the last decade an in-depth investigation of the interplay between pinning landscape and motif symmetry [16], influence of pinning size and period [17–20], competition between ordered and disordered defects [21–23], or pinning energy dispersion [24, 25], to name a few.

It has been recognized that vortex traps arranged in complex units cells such as honeycomb or kagomé patterns [26, 27], exhibit some properties unique to them. Indeed, (i) molecular dynamics simulations have revealed multistage melting of vortex ground states in a kagomé periodic array of pinning sites when the temperature is slowly varied [28], (ii) commensurate pinning enhancement taking place at magnetic fields $H/H_1{=}n/2$ (honeycomb) and $H/H_1{=}n/3$ (kagomé) rather than the standard $H/H_1{=}n$ [29], (iii) stronger enhancement of the depinning current compared to a triangular lattice [29], (iv) spontaneous transverse voltage and jamming effect in a honeycomb array generated by the dimerization of interstitial vortices [30], and (v) vortex interaction enhanced saturation number and caging effect [31]. Although a great theoretical effort has been undertaken to understand the physics of these systems, the experimental investigations remain scarce. The few performed experiments relied on electrical transport measurements and, therefore, represent an indirect assessment of the actual dynamics of the vortex matter[26, 31]. In addition, thermodynamic entropy is determined by measurements of heat, while much less common is the determination of configurational entropy. The latter relies on counting the available states, which is possible for systems where experimental techniques can resolve the state of the individual particles. This direct imaging of configurational entropy has been successfully done in magnetic systems[8, 9]. Bearing in mind the aforementioned flexibility of a vortex system, this opens a new route to explore degeneracy and frustration in nanostructured superconductors.

In this work we explore the vortex distribution, using scanning Hall probe microscopy (SHPM), in a thin superconducting film with a kagomé lattice consisting of elongated antidots (see Fig. 1(a)). By performing consecutive field-cooling (FC) experiments we can visualize the resulting vortex distributions at different fractional matching fields. The main observation is that each FC experiment at a fixed magnetic field value (between 0 and H_1) results in a different vortex configuration. This experimental irreproducibility indicates that a large set of vortex distributions exist with nearly the same en-

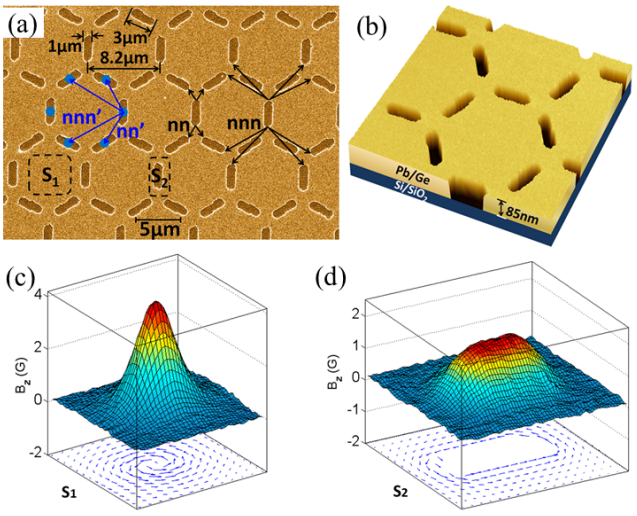

FIG. 1. Scanning electron micrograph (a) and atomic force microscopy image (b) of the investigated Pb film with an artificial kagomé lattice of elongated antidots. Experimentally obtained out-of-plane component of the magnetic field, B_z, and simulated current lines for an interstitial vortex located in the area $\mathtt{S}_1$ (c) and pinned vortex in area $\mathtt{S}_2$ (d). $\mathtt{S}_1$ and $\mathtt{S}_2$ are indicated in panel (a).

ergy. The resulting vortex patterns can be explained by the particular design of the elongated antidot structure and its impact on the different vortex-vortex interactions. Firstly, the short-range interaction between vortices located in two neighbouring antidots is enhanced due to the elongated shape of the antidots. This gives rise to very strong local constraints. In addition, the interaction between vortices separated by exactly one antidot ("long-range" interaction) is weaker and unable to differentiate between the various vortex distributions. As such, the long-range order is lifted and the vortex patterns are ruled by the specific local constraints. Moreover, the obtained degeneracy can be easily tuned by varying the applied magnetic field, which makes it an ideal toy model to explore degeneracy in physical systems.

II. SAMPLE AND EXPERIMENTS

Figs. 1(a-b) show the kagomé lattice of elongated antidots in a 85 nm thick Pb film, fabricated using conventional electron-beam lithography, on a Si/SiO_2 substrate. The sample stage is cooled to 77 K, using liquid nitrogen, to ensure a homogeneous growth. A Ge layer with thickness of 10 nm is also deposited on top of the Pb layer to protect it from oxidation. The source materials are 99.999%-pure Pb and 99.9999%-pure Ge. The external magnetic field is applied perpendicularly to the sample surface and the vortex configurations are directly visualized using a low temperature SHPM (with magnetic field resolution of 10^{-5} T and temperature stability better than 1 mK) [32, 33]. All the SHPM images of vortex patterns in our measurements are obtained by lifting the Hall cross about 500-800 nm above the sample surface at $T = 4.25$ K.

In analogy to other well-studied antidot systems [34, 35], the elongated antidots act as pinning centers to trap vortices. Since the attractive vortex-pinning force is much stronger than the repulsive vortex-vortex interaction, the vortices prefer occupying vacant antibars rather than forming an Abrikosov lattice. Figs. 1(c-d) show the experimentally obtained magnetic field profiles and the simulated current lines for an interstitial and trapped vortex, respectively. These results clearly indicate that the pinned vortex is strongly deformed. As a result, the interaction between vortices will dependent on their exact orientation. The short-range interaction, between vortices located at neighboring antidots is very strong and will introduce strict, magnetic field dependent, constrictions on the vortex lattice. For example, the amount of vortices observed in each unit cell perfectly coincides with the applied field value at $H = H_1/3$, $2H_1/3$ and H_1.

At fields below H_1 also a long-range interaction, between vortices separated by an empty antidot, plays an important role in determining the energy of the vortex lattice. Previous SHPM experiments on nanostructured Pb superconductors, in this field range, show that the observed vortex distributions are the ones maximizing the inter-vortex distance[36, 37]. In the present case, the anisotropy of the pinned vortices and the anisotropy of the superconducting film due to the kagomé antidot lattice results in a complex vortex-vortex interaction. Its impact on the final vortex distribution, given by the lowest energy state, is difficult to predict. Therefore, ~~one has to perform~~ TDGL simulations in order to gain insight and resolve the important ingredients determining the experimentally observed distributions.

III. THEORETICAL FORMALISM

The simulating results in this work are derived based on the time-dependent Ginzburg-Landau (TDGL) equations, which provide a very useful tool for simulating both dynamic and static superconducting problems. The normalized TDGL equations can be written as [39–41],

$$\partial_t \psi = (\nabla - i\mathbf{A})^2 \psi + \psi - |\psi|^2 \psi \tag{1}$$

$$\sigma \partial_t \mathbf{A} = \mathbf{J}_s - \kappa^2 \nabla \times \nabla \times \mathbf{A} \tag{2}$$

$$\mathbf{J}_s = \mathtt{Im}(\psi^* \nabla \psi) - \mathbf{A}|\Psi|^2 \tag{3}$$

where ψ, $\mathbf{A}$ and J_s are order parameter, vector potential and supercurrent density, respectively. The length is made dimensionless in units of coherence length ξ, time in ξ^2/D where D is diffusion coefficient, order parameter

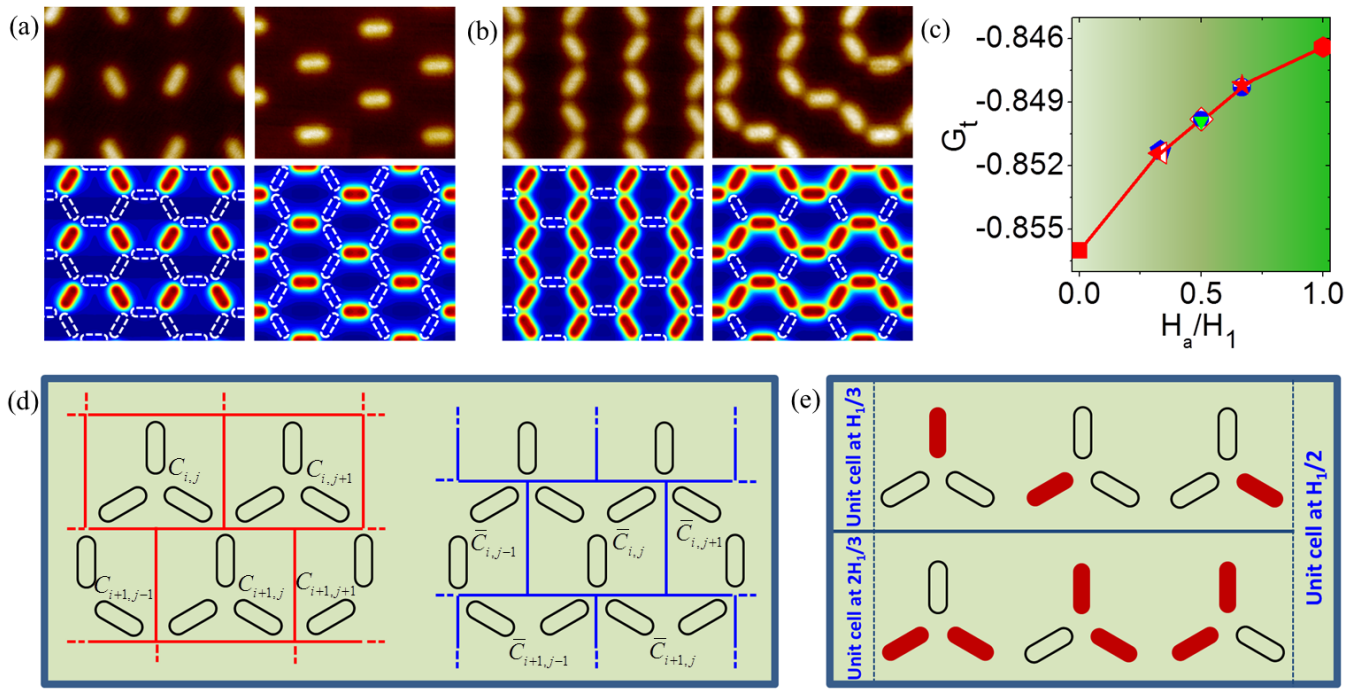

FIG. 2. (a-b) Two SHPM images (upper panels) and TDGL simulations (lower panels) of the vortex states in a kagomé antibar lattice at H_a=$H_1/3$ and $2H_1/3$, respectively. (c) Free energy corresponding to H_a =0 (red square), the two vortex states shown in panel (a) at $H_1/3$ (red-white triangle and blue pentagon), the three vortex states at $H_1/2$ shown in Fig. 4(b) (white diamond, blue circle and green triangle), the two vortex states shown in panel (b) at $2H_1/3$ (red pentagram and white-blue circle) and, finally, the vortex state shown in Fig. 5(b) at H_1 (red hexagon). (d) The discrete unit cells (red) and conjugated unit cells (blue) in the kagomé lattice. (e) Schematic representation of possible vortex arrangements in a unit cell at H_a=$H_1/3$, $2H_1/3$ and $H_1/2$.

in $\psi_0 = \sqrt{|a|/b}$, and vector potential in $\sqrt{2}\kappa H_c\xi$ where $H_c = \sqrt{4\pi a^2/b}$.

The magnetic field can be derived by Biot-Savart law,

$$\mathbf{B}(\mathbf{r}) = \frac{\mu_0}{4\pi}\int_V \frac{\mathbf{J}_s(\mathbf{r}')\times(\mathbf{r}-\mathbf{r}')}{|\mathbf{r}-\mathbf{r}'|^3}d\mathbf{r}' \qquad (4)$$

where $\mathbf{r}$=(x, y, h), $\mathbf{r}'$=(x', y', 0) and h is the distance between the Hall cross and sample surface. The Gibbs free energy density of the system, in units of $H_c^2V/8\pi$, can be calculated by [40]

$$G_t = G_h + G_p = V^{-1}\int_V [2(\mathbf{A}-\mathbf{A}_0)\mathbf{J}_s - |\psi|^4]d\mathbf{r} \qquad (5)$$

where $\mathbf{A}_0$ is the vector potential of the uniform magnetic field. We consider an infinite sample, and periodic boundary conditions are applied in the simulations. Because the thickness of the sample is sufficiently small, the variations of order parameter and currents along the thickness are neglected in simulations. To mimic the stable vortex patterns in the field-cooling experiments, we start the simulations from different randomly generated initial conditions [11]. Then we can obtain many vortex ground- and metastable states. We find that the free energy of some vortex states are nearly the same, and these vortex configurations agree well with the experimental vortex patterns at specific applied magnetic fields.

IV. RESULTS AND DISCUSSIONS

In order to show the presence of degeneracy and obtain the constraints, imposed by this particular system, we explore the vortex patterns at different fractional matching fields. Figs. 2(a-b) show two distinct SHPM images and TDGL simulations of typical vortex states observed at H_a=$H_1/3$ and $2H_1/3$, respectively. A good agreement is observed between the simulated results (lower panels) and the experimentally obtained data (upper panels). Moreover, the square versus triangular packing of the vortex lattice (shown in Fig. 2(a)) results in a distinct average vortex-vortex distance between both states. However, the observation of both vortex states indicates that the difference between the vortex interactions in the two states is too small to resolve between them. Naively, one could argue that the interaction in the square lattice is more efficiently screened than in the triangular lattice because of the appearance of an elongated antidot in between vortices in the latter case. This can be clarified by removing the vacant elongated antidots in between vortices. Indeed, the TDGL simulations indicate that the antidots effectively decrease the difference induced by the long-range interactions between the square and triangular vortex pattern. At $2H_1/3$ the interpretation is analogous. The interactions between the nearest-neighbor

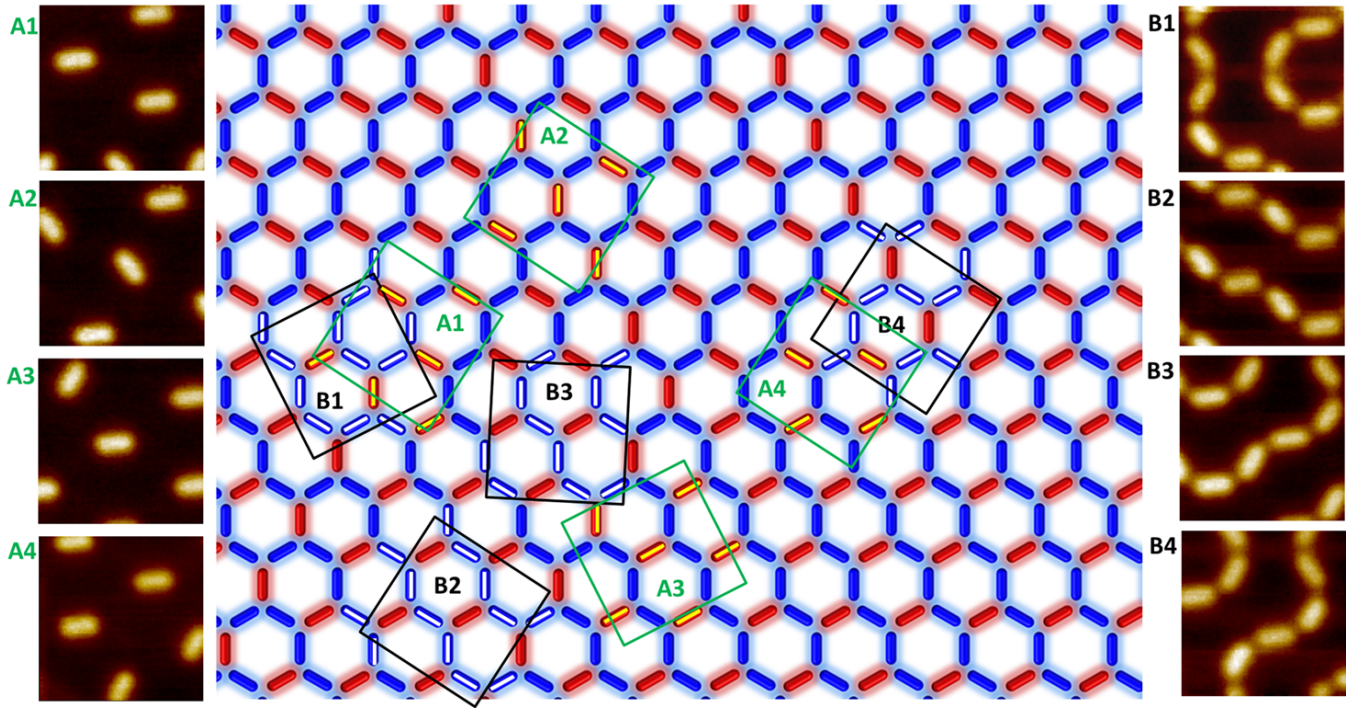

FIG. 3. Schematic representation of a possible degenerate vortex state constructed based on degeneracy rules at H_a=$H_1/3$ and $2H_1/3$ (middle panel). The red bars represent the vortex configuration at $H_1/3$, and the blue bars represent the vortex state at $2H_1/3$. Experimental vortex states at $H_1/3$ (left panels A1, A2, A3 and A4) and $2H_1/3$ (right panels B1, B2, B3 and B4), which exactly correspond to the local vortex patterns (red bars with yellow lines in four green boxes to the vortex configurations in left panels and blue bars with white lines in four black boxes to the vortex configurations in right panels) in the middle panel by rotating the boxes with about 30°, 90°, 150°, 210°, 270°, 330°.

vortices determine strong local constraints, while very small energy differences (about ten thousandth in units of $H_c^2V/8\pi$) exist between the vortex states arising from the interactions between vortices located at next-nearest neighboring antidots. In addition, we have calculated the free energy as a function of magnetic field, based on the TDGL simulations (see Fig. 2(c)). The free energy for different vortex distributions, marked by different symbols, is indeed nearly the same. These results show that the long-range interaction is unable to resolve between different distributions. The free energy of vortex states at $H_1/2$ is situated at midpoint between the vortex states at $H_1/3$ and $2H_1/3$ since the energy caused by vortex-vortex interactions increases linearly with external applied field.

By carefully analyzing the obtained experimental and simulated vortex patterns, we can identify common topological characteristics regarding the resulting vortex configurations. At H_a=$H_1/3$, exactly one third of the antidots are filled with vortices. By imposing homogeneity of the equilibrium state, this constraint persists on a local scale, which results in the occupation of one antidot at each vertex of the system. This constraint is a natural consequence of a FC experiment, since vortices are formed staring from a homogeneous field distribution. At H_a=$2H_1/3$ exactly the complementary conditions are fulfilled: (i) exactly two thirds of the elongated antidots are filled and (ii) two antidots are occupied at each unit cell of the system. As seen in the Fig. 2(b), these constraints result in the formation of parallel vortex strings at $2H_1/3$, which looks like the domain walls of the superconductor.

The topological characteristics of the different degenerate vortex patterns can be deduced from simple filling rules imposed onto the occupation of the kagomé lattice unit cell. This approach will allow us to calculate the degeneracy as a function of the applied magnetic field. As shown in Fig. 2(d), the kagomé lattice can be divided into unit cells and conjugated unit cells, which are labelled as $C_{i,j}$ and $\overline{C}_{i,j}$ respectively. The matrix $\mathbf{C}$=$[C_{i,j}]$ and $\overline{\mathbf{C}}$=$[\overline{C}_{i,j}]$ denote the number of vortices in each unit cell and conjugated unit cell. The aforementioned constraints can now be explicitly written down for both magnetic field values. In order to match the applied magnetic field the $\sum_{i,j}\{C_{i,j}\}$=$N/3$ at $H_1/3$ and the $\sum_{i,j}\{C_{i,j}\}$=$2N/3$ for $2H_1/3$, with N the amount of unit cells in the sample. As a result of the second (local) constraint, $C_{i,j}$ has to be 1 at $H_1/3$, one-occupied/two-empty antidots, and 2 at $2H_1/3$, two-occupied/one-empty antidot, which are reminiscent to ice rules [10–12]. Fig. 2(e) schematically presents the 3, equivalent, vortex arrangements in case $C_{i,j}=1$ and $C_{i,j}=2$.

If the adjacent unit cells are non-interacting the vortex distribution is highly degenerate and the amount of degeneracy for both field values is 3^N. In the case of a long-range interaction the translational symmetry will be preserved and only 3 possible distributions exist. As such no real degeneracy (i.e. scaling with N) can be observed. However, in the case of a short-range interaction the constraints are weakened and degeneracy is not fully lifted in this system. The nearest neighbor interaction adds an additional constraint to the conjugated unit cells. More specifically, each conjugated unit cell must contain one vortex at $H_1/3$, i.e. $\overline{C}_{i,j}$=1 and two vortices at $2H_1/3$, i.e., $\overline{C}_{i,j}$. Although it reduces the amount of degeneracy, this constraint is much weaker than that imposed by the long-range interaction. Based on our numerical calculations the amount of degenerate vortex states is $Z<1.644^N$ (see Supplementary Material [42]).

Moreover, with the aforementioned rules we can easily construct a possible vortex distribution on a larger scale. The middle panel of Fig. 3 shows a design of the vortex distribution in large area, in which red bars represent the vortex pattern at H_a=$H_1/3$, and blue bars represent the vortex pattern at $2H_1/3$. Please note that the reverse vortex patterns at $H_1/3$ turn out to be vortex states at $2H_1/3$ and vice versa. By comparing this pattern with a variety of SHPM images at both magnetic field values (upper and bottom panels of Fig. 2(e)) we can indeed confirm that all obtained vortex distributions are reproduced by these simple rules. Due to the symmetry of hexagon, we can get the same view of the sample with the graph under SHPM (left and right panels) by rotating the schematic with about 30°, 90°, 150°, 210°, 270°, 330°.

As mentioned above, the number of particles can be simply tuned by merely increasing or decreasing the external magnetic field. In virtue of this advantage, we also explore the vortex state degeneracy at $H_1/2$. As shown in Fig. 4(a), we observe a completely different vortex state at H_a=$H_1/2$. To understand better the apparent randomness of the vortex distribution, we also perform numerical TDGL simulations for the vortex states at the corresponding field H_a=$H_1/2$. Fig. 4(b) shows the numerical simulating vortex states, which clearly resemble the vortex patterns observed by SHPM. Moreover, the TDGL simulations indicate that the free energy of these different vortex states are the same (see Fig. 2(c)).

Let us now identify the topological characteristics of the different degenerate vortex patterns in Figs. 4(a) and 4(b). Firstly, since the applied magnetic field is $H_1/2$ and a FC procedure was used, only half of the antidots are occupied with vortices and the remaining half are empty. Secondly, the tendency of the system to keep a homogeneous field distribution results in the absence of completely empty unit cells and completely filled unit cells. As a result $C_{i,j}$ has to be 1, one-occupied/two-empty antidots, or 2, two-occupied/one-empty antidot, which are reminiscent to ice rules. The obtained patterns are a combination of the 6 building blocks (presented in Fig. 2(e)) used to construct the vortex distribution at H_a=$H_1/3$ and H_a=$2H_1/3$. In this case, we can easily pinpoint the initial constraints, $1\leq C_{i,j}\leq 2$ and $\sum_{i,j}\{C_{i,j}-1\}=N/2$. It is interesting to note that the reverse patterns of vortex states at $H_1/2$ are also degenerate vortex states. For instance, as shown in Fig. 4(b), the vacant antibars (white dash bars) are also degenerate vortex states at $H_1/2$. If no interaction exists between these unit cells, the aforementioned constraints results in an amount of degeneracy equal to $Z=\frac{3^N\cdot N!}{((N/2)!)^2}$. Based on Stirling's approximation, $Z\approx\sqrt{\frac{2}{\pi N}}\cdot 6^N$ (see Supplementary Material [42]). However, also at this magnetic field value two additional constraints appear due to the interplay between neighboring unit cells. These constraints can be well identified using the conjugated unit cells: (i) Similar to the regular unit cells, there must be 1 or 2 vortices in every conjugated unit cell, i.e., $1\leq\overline{C}_{i,j}\leq 2$. (ii) The number of conjugated unit cells with one vortex must be $N/2$, i.e., $\sum_{i,j}\{\overline{C}_{i,j}-1\}=N/2$.

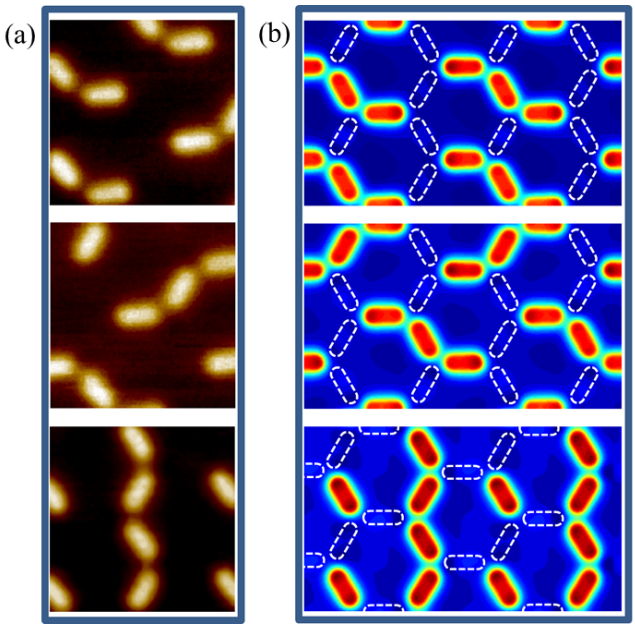

FIG. 4. (a) Experimental SHPM images of three different degenerate vortex states in a kagomé lattice of elongated antidots at an applied field H_a=$H_1/2$. (b) Three simulated vortex states at the same magnetic field value.

Finally, a general constraint was observed, combining both the regular and conjugated unit cells, in order to avoid the accumulation of one-vortex-unit-cells or two-vortex-unit-cells in a larger area (overall uniformity of the magnetic field profile), every unit cell and its three conjugated unit cells (also every conjugated unit cell and its three unit cells) are neither all two-vortex-unit-cells nor all one-vortex-unit-cells based on the experimental and simulating vortex patterns (see Fig. 4), i.e., $5\leq C_{i,j}+\overline{C}_{i-1,j}+\overline{C}_{i,j-1}+\overline{C}_{i,j}\leq 7$, $5\leq\overline{C}_{i,j}+C_{i,j}+C_{i,j+1}+C_{i+1,j}\leq 7$. Because of these con-

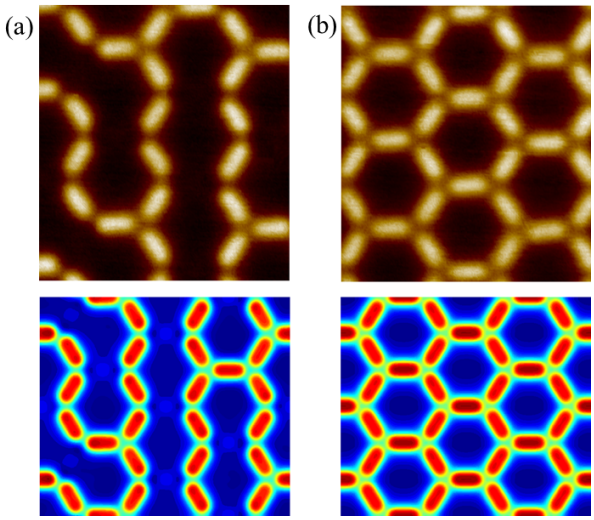

FIG. 5. (a-b), Experimental observation of vortex states in kagomé antibar latice at H_a=0.792 G (between $2H_1/3$ and H_1) and H_a=H_1 via SHPM. (c), Numerical simulating vortex state at H_a=0.801 G, which is very close to external field in Fig. 4(a). (d), TDGL simulating vortex state at H_1.

straints, the amount of degeneracy is reduced. For example, the amount of degeneracy in 16 unit cells is Z<6.17×10^9 (see Supplementary Material [42]), which is much less than possible vortex states with 16 unit cells (5.54×10^{11}) in the non-interacting case. However, compared to H_a=$H_1/3$ or $2H_1/3$ the degeneracy is strongly increased at H_a=$H_1/2$.

It has been already well established that not all nanoscale ferromagnetic islands comply with ice rules in spin ice system. In vortex system, additional vortices (vortex-defects) can be introduced by detuning the external field. Fig. 5(a) shows the experimental SHPM vortex pattern at H_a=0.792 G ($0.741H_1$). Some of the vortex strings intersect at some vertices, where three neighbor antibars are all occupied by the vortices. Such defects will have an impact on the degeneracy of the total system. With increasing field, the amount of defects increases, and the superconducting stripes are divided into more isolated areas. The increasing number of defects cause a reduction of degeneracy of the vortex states. Finally, as shown in Fig. 5(b), at H_1 every antibar traps exactly one vortex to form a large vortex-net. The vortex state at H_1 is unique and degeneracy is completely suppressed.

V. CONCLUSION

In summary, we fabricated a kagomé lattice with elongated antidots. This structure permits us to boost the first neighbor interaction and directly observe many distinct degenerate vortex states with low temperature scanning Hall probe microscopy at several fractional matching fields. Based on the experimental measurements and TDGL simulations, we find the local degeneracy rules to characterize the vortex configurations at $H_1/3$, $H_1/2$ and $2H_1/3$, respectively. The local degeneracy rules can give rise to different vortex distributions and a large configuration entropy. In addition, the vortex-defects can result in a failure of the degeneracy rules and the decrease of vortex degeneracy. The elongated antidot system in the kagomé antibar lattice provides an entirely new way to study vortex degeneracy via SHPM directly and, as a first in its kind exploration, it shows the potential of similar vortex systems as a highly tunable playground to explore concepts like frustration and degeneracy.

Acknowledgments

C.X. and A.H. acknowledge the support by the Fundamental Research Funds for the Central Universities (No. G2016KY0305, 310812171011). Y.H.Z. C.X. and A.H. acknowledge the National Natural Science Foundation of China (No. 11421062) and the National Key Project of Magneto-Constrained Fusion Energy Development Program (No. 2013GB110002). J.Y.G, V.Z., J.V.V. and V.V.M. acknowledge the support from the Methusalem funding by the Flemish government and the Flemish Science Foundation (FWO-Vl).

xuecun@nwpu.edu.cn
junyi.ge@fys.kuleuven.be
joris.vandevondel@kuleuven.be

[1] C. N. Weiler, T. W. Neely, D. R. Scherer, A. S. Bradley, M. J. Davis, and B. P. Anderson, Nature (London) **455**, 948 (2008).
[2] J. R. Abo-Shaeer, C. Raman, J. M. Vogels, and W. Ketterle, Science **292**, 476 (2001).
[3] P. T. Korda, G. C. Spalding, and D. G. Grier, Phys. Rev. B **66**, 024504 (2002).
[4] P. Tierno, and T. M. Fischer, Phys. Rev. Lett. **112**, 048302 (2014).
[5] M. Berciu, T. G. Rappoport, and B. Jankó, Nature (London) **435**, 71 (2005)
[6] T. Richter, C. Blömers, H. Lüth, R. Calarco, M. Indlekofer, M. Marso, and T. Schäpers, Nano Lett. **8**, 2834 (2008)
[7] N. Poccia, T. I. Baturina, F. Coneri, C. G. Molenaar, X. R. Wang, G. Bianconi, A. Brinkman, H. Hilgenkamp, A. A. Golubov, V. M. Vinokur, Science **349**, 1202 (2015).
[8] R. F. Wang, C. Nisoli, R. S. Freitas, J. Li1, W. McConville, B. J. Cooley, M. S. Lund, N. Samarth, C. Leighton, V. H. Crespi and P. Schiffer, Nature **439**, 303 (2006)
[9] P.l E. Lammert, X. Ke, J. Li, C.o Nisoli, D.d M. Garand, V. H. Crespi and P. Schiffer, Nature Physics **6**, 786 (2010)
[10] A. Libál, C. J. Olson Reichhardt, and C. Reichhardt,

Phys. Rev. Lett. **102**, 237004 (2009).
[11] M. L. Latimer, G. R. Berdiyorov, Z. L. Xiao, F. M. Peeters, and W. K. Kwok, Phys. Rev. Lett. **111**, 067001 (2013).
[12] P. A. McClarty, A. O'Brien, and F. Pollmann, Phys. Rev. B, **89**, 195123 (2014).
[13] S. Seki, X. Z. Yu, S. Ishiwata, and Y. Tokura, Science **336**, 198, (2012).
[14] J. Sampaio, V. Cros, S. Rohart, A. Thiaville, and A. Fert, Nature Nanotech. **8**, 839 (2013).
[15] O. Romero-Isart, C. Navau, A. Sanchez, P. Zoller, and J. I. Cirac, Phys. Rev. Lett. **111**, 145304 (2013).
[16] R. B. G. Kramer, A.V. Silhanek, J. Van de Vondel, B. Raes, and V. V. Moshchalkov, Phys. Rev. Lett. **103**, 067007 (2009).
[17] A. V. Silhanek, W. Gillijns, M. V. Milošević, A. Volodin, V. V. Moshchalkov, and F. M. Peeters, Phys. Rev. B **76**, 100502(R) (2007).
[18] M. Motta, F. Colauto, W. A. Ortiz, J. Fritzsche, J. Cuppens, W. Gillijns, V. V. Moshchalkov, T. H. Johansen, A. Sanchez and A. V. Silhanek, Appl. Phys. Lett. **102** 212601 (2013).
[19] D. Ray, C. J. Olson Reichhardt, B. Jankó and C. Reichhardt, Phys. Rev. Lett. **110**, 267001 (2013).
[20] Y. L. Wang, M. L. Latimer, Z. L. Xiao, R. Divan, L. E. Ocola, G. W. Crabtree and W. K. Kwok, Phys. Rev. B **87** 220501(R) (2013).
[21] C. J. Olson, C. Reichhardt, and S. Bhattacharya, Phys. Rev. B **64**, 024518, (2001).
[22] G. Pasquini, D. Pérez Daroca, C. Chiliotte, G. S. Lozano, and V. Bekeris, Phys. Rev. Lett. **100**, 247003 (2008).
[23] Y. L. Wang, L. R. Thoutam, Z. L. Xiao, B. Shen, J. E. Pearson, R. Divan, L. E. Ocola, G. W. Crabtree, and W. K. Kwok, Phys. Rev. B **93**, 045111 (2016).
[24] J. Gutierrez, A. V. Silhanek, J. Van de Vondel, W. Gillijns, and V. V. Moshchalkov, Phys. Rev. B **80**, 140514(R) (2009).
[25] G. Grimaldi, A. Leo, A. Nigro, A. V. Silhanek, N. Verellen, V. V. Moshchalkov, M. V. Milošević, A. Casaburi, R. Cristiano, and S. Pace, Appl. Phys. Lett. **100**, 202601 (2012).
[26] T. C. Wu, J. C. Wang, L. Horng, J. C. Wu, and T. J. Yang, J. Appl. Phys. **97**, 10B102 (2005).
[27] J. Cuppens, G. W. Ataklti, W. Gillijns, J. Van de Vondel, V. V. Moshchalkov, and A. V. Silhanek, J. Supercond. Nov. Magn. **24**, 7 (2011).
[28] M. F. Laguna, C. A. Balseiro, D. Dominguez, and F. Nori, Phys. Rev. B **64**, 104505 (2001).
[29] C. Reichhardt, and C. J. Olson Reichhardt, Phys. Rev. B **76**, 064523 (2007).
[30] C. Reichhardt, and C. J. Olson Reichhardt, Phys. Rev. Lett. **100**, 167002 (2008).
[31] M. L. Latimer, G. R. Berdiyorov, Z. L. Xiao, W. K. Kwok, and F. M. Peeters, Phys. Rev. B **85**, 012505 (2012).
[32] J. Y. Ge, J. Gutierrez, V. N. Gladilin, J. T. Devreese, and V. V. Moshchalkov, Nature Commun. **6**, 6573 (2015).
[33] B. Raes, J. Van de Vondel, A. V. Silhanek, C. C. de Souza Silva, J. Gutierrez, R. B. G. Kramer, and V. V. Moshchalkov, Phys. Rev. B **86**, 064522 (2012).
[34] X. Hallet, M. Mátéfi-Tempfli, S. Michotte, L. Piraux, J. Vanacken, V. V. Moshchalkov, and S. Mátéfi-Tempfli, Small **5**, 2413 (2009).
[35] V. V. Moshchalkov, M. Baert, V. V. Metlushko, E. Rosseel, M. J. Van Bael, K. Temst, R. Jonckheere, and Y. Bruynseraede, Phys. Rev. B **54**, 7385 (1996).
[36] C. C. de Souza Silva, B. Raes, J. Brisbois, L. R. E. Cabral, A. V. Silhanek, J. Van de Vondel and V. V. Moshchalkov Phys. Rev. B **94**, 024516 (2016)
[37] J. Gutierrez, B. Raes, J. Van de Vondel, A. V. Silhanek, R. B. G. Kramer, G. W. Ataklti, and V. V. Moshchalkov, Phys. Rev. B **88**, 184504 (2013).
[38] J. Pearl, Appl. Phys. Lett. **5**, 65 (1964).
[39] Gropp, W. D. et al. Numerical simulation of vortex dynamics in type-II superconductors. J. Comput. Phys. **123**, 254-266 (1996).
[40] Schweigert, V. A. & Peeters, F. M. Phase transitions in thin mesoscopic superconducting disks. Phys. Rev. B **57**, 13817-13832 (1998).
[41] Winiecki, T. & Adams, C. S. A fast semi-implicit finite-difference method for the TDGL equations. J. Comput. Phys. **179**, 127-139 (2002).
[42] See Supplemental Material for more detail analysis on the amount of degeneracy at $H_1/3$, $2H_1/3$ and $H_1/2$.